

Nanocrystal Formation in Si Implanted Thin SiO_2 Layers under the Influence of an Absorbing Interface

T. Müller,* K.-H. Heinig, and W. Möller

Forschungszentrum Rossendorf, Institut für Ionenstrahlphysik
und Materialforschung, PO-BOX 51 01 19, 01314 Dresden, Germany

(Dated: 19th August 2018)

Kinetic 3D lattice Monte Carlo studies are presented on Si nanocrystal (NC) formation by phase separation in 1 keV Si^+ implanted thin SiO_2 films. The simulation start from Si depth profiles calculated using the dynamic, high-fluence binary collision code TRIDYN. From the initial Si supersaturation, NCs are found to form either by nucleation, growth and Ostwald ripening at low Si concentrations. Or at higher concentrations, non-spherical, elongated Si structures form by spinodal decomposition, which spheroidize by interface minimization during longer annealing. In both cases, the close SiO_2/Si interface is a strong sink for diffusing Si atoms. The NCs align above a thin NC free oxide layer at the SiO_2/Si interface. Hence, the width of this zone denuded of NCs has just the right thickness for NC charging by direct electron tunneling, which is crucial for non-volatile memory applications. Moreover, the competition of Ostwald ripening and Si loss to the interface leads at low Si concentrations (nucleation regime) to a constant width of the denuded zone and a constant mean NC size over a long period of annealing.

I. INTRODUCTION

Nanocrystals (NCs) embedded in a matrix are known to form by phase separation of a supersaturated solid solution. At low impurity concentrations, nucleation [1] and conservative Ostwald ripening [2] will lead to an coarsening ensemble of precipitates during annealing. According Lifshitz, Slyozov, and Wagner [3, 4], the mean particle size increases according a power law in time. At higher concentrations, phase separation takes place by spinodal decomposition [5]. A vanishing nucleation barrier [6] implies that small initial concentration fluctuations amplify during the annealing. Non-spherical structures precipitate, which form a connected network of precipitates above the percolation threshold [7]. In the presence of an absorbing (reflecting) interface phase separation is considerably altered. For spinodal decomposition, it is known that the interface directs the wave vector of concentration fluctuations [8]. Hence, a layered structure of precipitates forms close to the interface. Recent studies also revealed an influence on nucleation, which can either be enhanced or depressed by the absorbing/reflecting interface [9].

Phase separation in thin films is of particular interest for the fabrication of non-volatile memories based on MOS transistors containing semiconductor NCs in their gate oxide [10]. Using especially 1 keV Si^+ implantation into 8 nm thick SiO_2 on (001)Si, NCs were formed a few nanometers above the Si/SiO_2 interface [11], which is in direct tunneling distance. Thus, these NCs can be charged by direct electron tunneling from the Si, which is a prerequisite for a high endurance and low operation voltages of NC-memories [12]. Nevertheless, the influence of the absorbing SiO_2/Si interface on Si NC formation is not well understood and requires further investigations. For that aim, kinetic 3D lattice Monte Carlo (KMC) simulations of Si phase separation from SiO_2 were reported

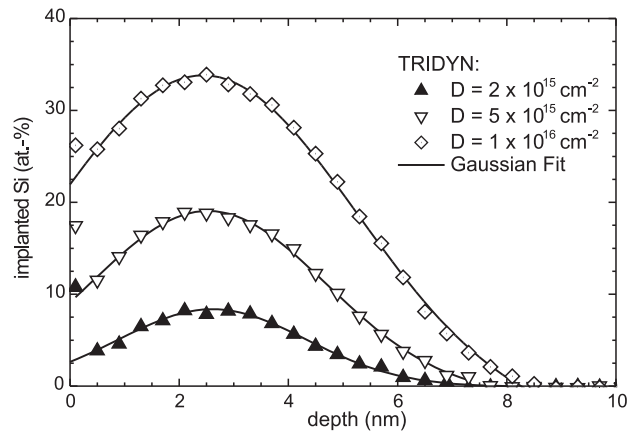


Figure 1: TRIDYN depth profiles for 1 keV Si^+ implantation into SiO_2 (denoted by open and bold symbols). The profiles were fitted to Gaussian distributions (Table I) shown as solid curves.

recently[13] and shall be discussed in more detail in this paper. As input data, Si depth profiles for 1 keV Si^+ implantation into SiO_2 were taken from dynamic, high-fluence binary collision simulations conducted with TRIDYN [14].

II. BINARY COLLISION SIMULATION OF HIGH FLUENCE Si^+ IMPLANTATION

The TRIDYN depth profiles of implanted Si into of SiO_2 are shown in Fig. 1 for 1 keV energy. Similar to the widely applied binary collision simulation code TRIM [15], TRIDYN is used to calculate ion range profiles in amorphous targets but includes additionally dynamic target changes as induced by sputtering, swelling and ion beam mixing. The input parameters being required include the displacement and surface binding energies of the target atoms. For both, Si and O, the displacement energy was assumed to be 8 eV. The surface binding energies of Si and O are assumed to vary linearly with

*T.Mueller@fz-rossendorf.de; Tel. +49 351 260 3148; Fax. +49 351 260 3285; <http://www.fz-rossendorf.de>

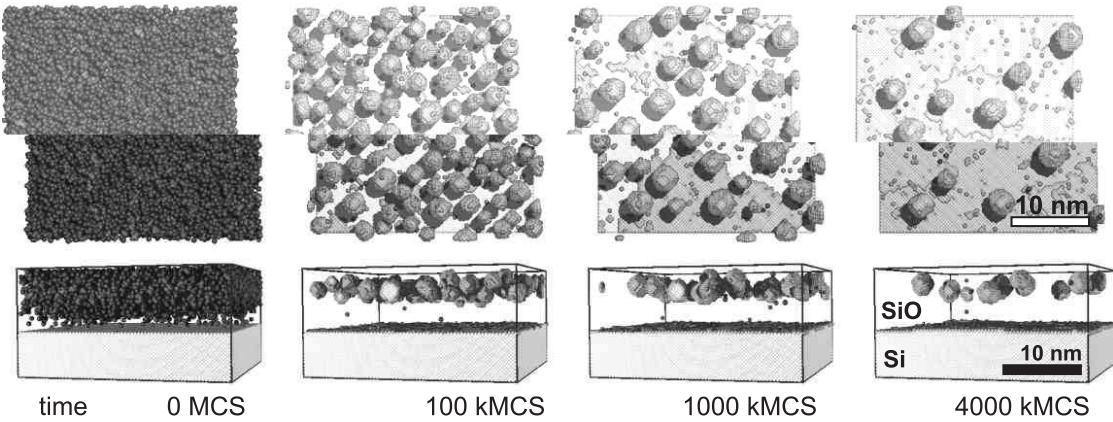


Figure 2: Snapshots of KMC simulations (top view and cross section) of phase separation in 8 nm thick SiO_2 on (001) Si implanted with Si. The initial Si depth profile was taken from Fig. 1 for a fluence of $2 \times 10^{15} \text{ cm}^{-2}$. Phase separation proceeds via nucleation and growth.

the surface composition that they balance the enthalpies of sublimation and decomposition of Si and SiO_2 , respectively [16, 17].

The Si depth profile broadens with increasing fluence due to swelling, sputtering and mixing (Fig. 1). Additionally, preferential sputtering has lead to a Si enrichment at the target surface. Nevertheless, the profile shape remains Gaussian in the fluence range considered here. The parameters of Gaussian distributions fitted to the TRIDYN profiles of Fig. 1 are summarized in Table I, which also includes the calculated target swelling.

III. THE KINETIC MONTE CARLO METHOD

The implanted Si separates from the SiO_2 matrix during subsequent annealing, i.e. precipitates are formed. In general, this process of phase separation consists of a huge number of elementary events (like bond breaking, diffusional jumps of atoms, chemical reactions etc.) that occur in random sequence. Their simulation must take into account both energetic and statistical aspects, which is here suitably conducted by kinetic 3D lattice Monte Carlo (KMC) simulations. The KMC method applied is discussed elsewhere in detail [18], a short overview will be given instead.

The kinetics of Si atoms is described in a solid host ma-

Table I: Parameters of Gaussian distributions fitted to TRIDYN profiles of Fig. 1. Additionally, the target swelling d_{swelling} due to incorporated Si ions is given.

ion fluence (10^{15} cm^{-2})	2	5	10
projected range R_p (nm)	2.6	2.5	2.4
range straggling σ (nm)	1.8	2.3	3.0
peak concentration c_{max} (at.-%)	9	19	34
target swelling d_{swelling} (nm)	0.2	0.6	1.3

trix (SiO_2), which is the background or "system's vacuum". Thereby, an underlying fcc lattice has been assumed, which together with hcp is the most isotropic lattice. Within this host dissolved Si diffuses and can form precipitates. (Crystallites obey the same four-fold symmetry than in the diamond lattice. The lattice spacing were chosen such that the correct atomic Si density is obtained.) Applying the classical lattice gas model with attractive Si-Si interaction, the energetics is determined by the nearest-neighbor (NN) Ising model. The kinetics of the system is governed by the Kawasaki particle exchange dynamics using the Metropolis algorithm [19]. Statistically, each Si atom is allowed to jump from an initial site i to an empty neighboring site f during one Monte Carlo step (MCS), which is the time unit of the KMC simulation. The transition probability P_{if} for one atom to jump is given by

$$P_{if} = \begin{cases} \tau_0^{-1} e^{-E_A \beta}, & n_f \geq n_i, \\ \tau_0^{-1} e^{-[E_A + (n_i - n_f)E_B] \beta}, & n_f < n_i, \end{cases}$$

where τ_0^{-1} denotes the attempt frequency, $n_{i,f}$ represents the number of NN bonds at the two sites and $\beta = (kT)^{-1}$ has its usual meaning. E_A is the diffusion barrier for Si in SiO_2 and E_B the Si-Si bond strength. In principle, the bond strength E_B can be determined from the solubility of Si in SiO_2 via the detailed balance of Si attachment/detachment at the Si/ SiO_2 interface. (It has to be taken into account that the coordination number in the fcc lattice of the simulation is 12 instead of 4 in the case of the Si lattice.) In kinetic Monte Carlo simulations it is convenient to renormalize the transition probability of the most probable event to one. For $E_A \rightarrow 0$ each diffusional jump is allowed, which defines the temperature dependent time scale of a Monte Carlo step (MCS), $\tau = \tau_0 \exp\{E_A \beta\}$. Then, the dimensionless transition probability reads as $\tilde{P}_{if} = \min(1, \exp\{-(n_i - n_f)E_B \beta\})$. Energetically unfavored events ($n_i > n_f$) are allowed, nevertheless, to occur by thermal activation according the Boltzmann statistics.

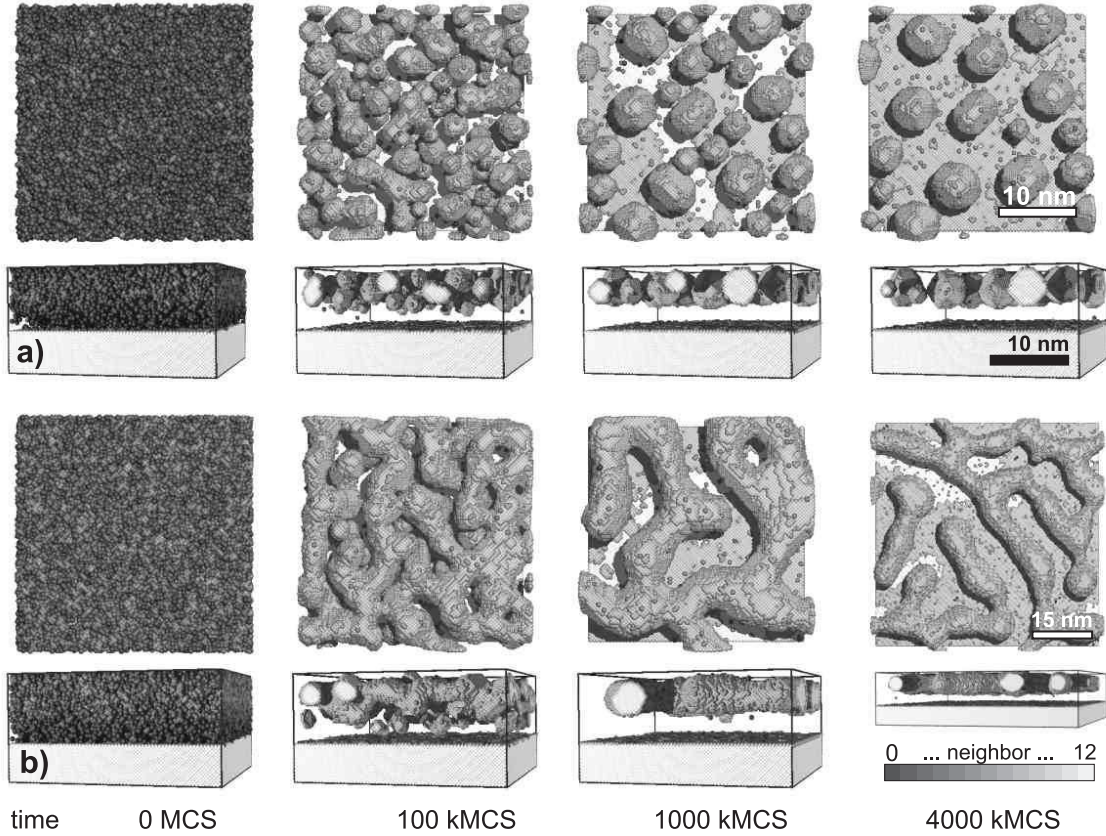


Figure 3: Snapshots of KMC simulations of phase separation in 8 nm thick SiO_2 on (001) Si implanted with Si. The initial depth profiles were taken according Fig. 1 for fluences of $5 \times 10^{15} \text{ cm}^{-2}$ (a) and $1 \times 10^{16} \text{ cm}^{-2}$ (b). Phase separation proceeds via spinodal decomposition (a,b) and is accompanied by percolation at the highest fluence (b). The 15 nm scale applies only in the lower right corner.

In principle, the scale of time and temperature of the simulation is given by the experimental parameters of the system under consideration. However, the diffusivity and the solubility of Si in SiO_2 are largely unknown, thus reduced units are applied for the time - the Monte Carlo step - and for the temperature - the reduced temperature $E_B\beta$. Nevertheless, the path of systems's evolution towards equilibrium predicted by KMC simulations may improve the process understanding substantially.

IV. KMC SIMULATIONS OF PHASE SEPARATION

In Fig. 2 and 3 snapshots of the KMC simulations of the phase separation are shown for $E_B\beta = 2$. Thereby, the TRIDYN profiles of Fig. 1 were used as initial Si distribution. The size of simulation volume is $56 \times 56 \times \Delta z \text{ nm}^3$, where Δz is 8 nm plus swelling due to implantation according Tab. I. For the sake of clarity, only a quarter of the simulation cell is shown in Fig. 2 and 3 besides of the lower right corner in Fig. 3. Periodic boundary conditions were applied in the plane, while at the surface a reflecting boundary conditions was applied. The simulation cell (SiO_2) borders on fixed (001) layers of Si atoms accounting for Si attachment/detachment at

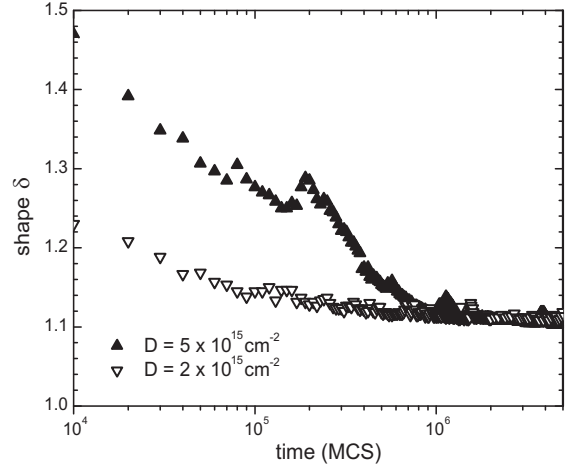


Figure 4: Evolution of mean NC shape measured by δ in the nucleation regime ($2 \times 10^{15} \text{ cm}^{-2}$) and for spinodal decomposition ($5 \times 10^{15} \text{ cm}^{-2}$). The highest fluence ($1 \times 10^{16} \text{ cm}^{-2}$) is omitted due to percolation.

the Si/SiO_2 interface, which is an effective sink for diffusing Si atoms.

Two regimes of phase separation are found by KMC simulations. A "nucleation and growth" regime is observed for $2 \times 10^{15} \text{ Si}^+ \text{cm}^{-2}$. Si NCs nucleate and grow further at the expense of Si supersaturation (Fig. 2, 100 kMCS). Later on, NCs grow by Ostwald ripening and finally dissolve due to Si loss to the SiO_2/Si interface, respectively. Above $5 \times 10^{15} \text{ Si}^+ \text{cm}^{-2}$ a "spinodal decomposition" regime is identified, where due to the vanishing nucleation barrier [6] non-spherical, elongated Si structures form (Fig. 3 a, 100 kMCS). At even higher Si concentrations ($1 \times 10^{16} \text{ Si}^+ \text{cm}^{-2}$), above the percolation threshold, these structures become laterally connected and extend over several tens of nanometers (Fig. 3 b, 100 kMCS).

As seen in Fig. 2 and 3, nucleation and spinodal decomposition lead to different initial shapes of precipitates, which can be accessed by defining a shape parameter δ [18] (analogously to the moment of inertia),

$$\delta = \frac{5}{3NR} \sum_{i=1}^N (\vec{r} - \vec{r}_i)^2.$$

It measures the mean squared distance of atoms from the center of mass of the NC relative to that of a sphere with radius R , which assumes that all N atoms within a NC form a sphere with $R = \sqrt[3]{(3N)/(4\pi)}$. Thus, the shape parameter δ should tend to one for a spherical NC. Non-spherical structures should obey $\delta > 1$. The time evolution of the shape parameter δ is shown in Fig. 4. In the nucleation regime, the NC shape deviates little from the spherical form ($\delta \approx 1.2$) at the beginning, while it approaches quickly a constant value of $\delta \approx 1.1$ during further annealing. (Small NC may have a δ slightly larger than one due to their faceted shape.) For spinodal decomposition δ the formed structures are considerably non-spherical ($\delta > 1.3$) initially. Below the percolation threshold, non-spherical Si precipitates evolve into spherical NCs ($\delta \rightarrow 1$) due to interface minimization, which can hardly be distinguished from NCs formed by nucleation (see Fig. 2 and 3 (a), 1000 kMCS).

The close SiO_2/Si interface acts as an effective sink for Si diffusing within the SiO_2 in both regimes, which results in a zone denuded of NCs formed at the interface. However, a more detailed consideration reveals differences between nucleation and growth and spinodal decomposition. As shown in Fig. 5, for the nucleation regime ($2 \times 10^{15} \text{ cm}^{-2}$) the width of the denuded zone is constant over a long period of annealing. A similar behavior is observed for the mean NC size (Fig. 6). The competition of NC dissolution due to Si loss to the interface and Ostwald ripening leads to a constant mean NC diameter.

On the other hand, the mean precipitate size is larger in the spinodal decomposition regime (Fig. 3). According the Gibbs-Thomson relation, the equilibrium Si solubility in SiO_2 at the precipitate's interface is lower than in the nucleation regime. Thus, the diffusional flux of Si from the precipitates towards the Si/SiO_2 interface is greatly reduced. Consequently, the NC diameter is still increasing. Within the annealing period shown in Fig. 6, Ostwald ripening is more effective than the Si loss to the SiO_2 interface. Moreover, interface min-

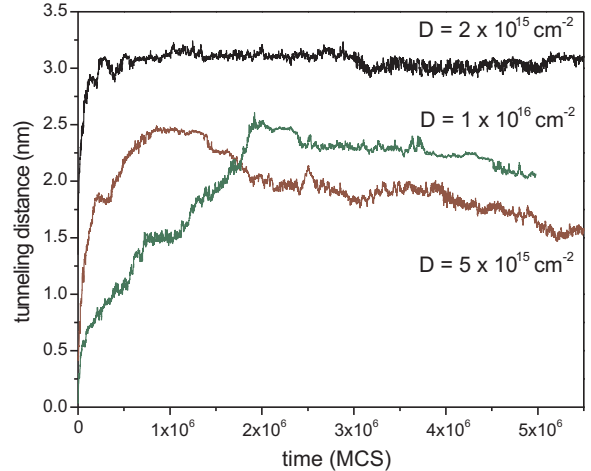


Figure 5: Width of the zone denuded of NCs between the SiO_2/Si interface and the NCs.

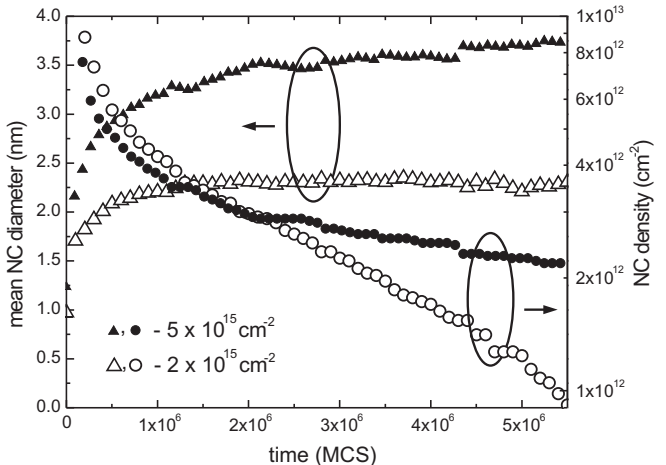


Figure 6: Evolution of the mean NC diameter and the NC density during annealing for fluences of $2 \times 10^{15} \text{ cm}^{-2}$ and $5 \times 10^{15} \text{ cm}^{-2}$. The highest fluence ($1 \times 10^{16} \text{ cm}^{-2}$) is omitted due to percolation.

imization of non-spherical precipitates leads to a narrowing of the denuded zone (Fig. 5).

In both regimes, NCs form at high density as shown in Fig. 6 if the percolation threshold is not reached. In the initial stage, the NC density is slightly higher in the nucleation regime, while during longer annealing the NC dissolve faster than in the spinodal regime.

For a fluence of $2 \times 10^{15} \text{ Si}^+ \text{cm}^{-2}$ (nucleation regime), the evolution of mean NC size and density is compared for phase separation in 8 nm and 20 nm thick SiO_2 (Fig. 7). For both case, the same ion energy of 1 keV and, thus, the same initial Si depth profiles were used. Up to an annealing time of 10^6 MCS, the NC size and density obeys the same power law for both oxide thickness (seen as straight line in the Log-Log plot of Fig. 7). The Si/SiO_2 interface does not influence the early NC evolution. Later on (> 1000 kMCS), NCs start to

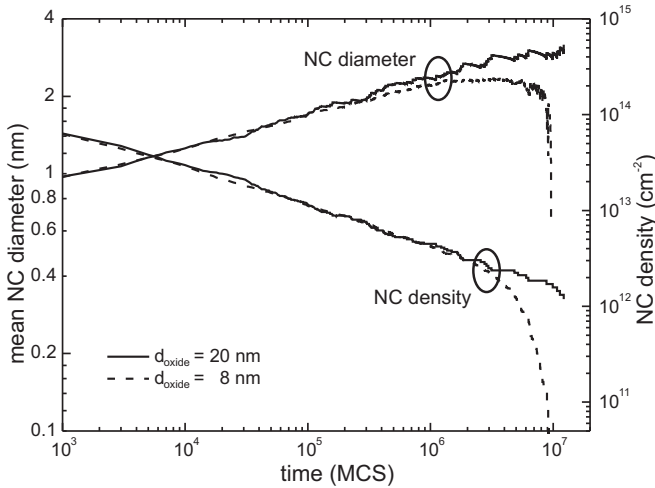


Figure 7: Comparison of mean NC size and density for phase separation in 8 nm and 20 nm thick SiO_2 layers implanted at a Si fluence of 2^{15} cm^{-2} .

dissolve in the 8 nm thick SiO_2 layer. Thus, the mean NC size becomes constant and NCs dissolve faster than by Ostwald ripening, which is seen as kink in the plot of the NC density after 2×10^6 MCS. The evolution of the NC size and density is not affected by the far SiO_2/Si interface in the case of the thick (20 nm) SiO_2 .

V. SUMMARY

Binary collision simulations of high fluence 1 keV Si^+ implantation into 8 nm thick SiO_2 were combined with kinetic 3D lattice Monte Carlo simulations of phase separation of

Si from SiO_2 . Two major regimes of phase separation, nucleation and growth, and spinodal decomposition were observed. At high concentrations, spinodal decomposition is accompanied by percolation. The regimes of phase separation determines the initial shape of the precipitates. Nucleation and growth leads to almost spherical NCs, while spinodal decomposition results in non-spherical Si structures, which may spheroidize during long lasting annealing.

The performed process simulations predict that for non-volatile memory applications Si NCs should be preferably synthesized in the nucleation regime. Then, NCs form at high density ($> 10^{12} \text{ cm}^{-2}$). The influence of the absorbing Si/SiO_2 interface leads to NC dissolution and a zone denuded of NC forms at the interface. This denuded zone has just the right thickness of 2...4 nm in order to act a barrier for NC charging by direct electron tunneling from the Si. Moreover in the nucleation regime, the width of this barrier is found to be constant over a long period of annealing. A similar behavior holds for the mean NC size. For spinodal decomposition, the situation is different. The width of the denuded zone and the mean NC size varies during annealing (Fig. 5 and 6). Above the percolation threshold, the formed elongated structures are connected laterally, and, therefore, would behave like a floating gate in a conventional MOS transistor. Charge brought to this network of precipitates would spread and one oxide defect could lead to a complete discharging of the floating gate, which could not occur in the case of laterally well-isolated Si NCs.

Acknowledgments

This work was sponsored by the European Community under the auspices of the GROWTH project. GRD1-2000-25619.

[1] J. H. Hollomon and D. Turnbull, *Prog. in Met. Phys.* **3** (1953).
[2] W. Ostwald, *Zeitschrift Phys. Chem.* **22** (1897).
[3] I. M. Lifshitz and V. V. Slyozov, *J. Phys. Chem. Solids* **19** (1961).
[4] C. Wagner, *Z. Elektrochem.* **65** (1961).
[5] J. W. Cahn, *Acta Metall.* **9** (1961).
[6] F. K. LeGoues, Y. W. Lee, and H. I. Aaronson, *Acta Metall.* **32** (1984).
[7] S. Hayward, D. W. Heermann, and K. Binder, *J. Stat. Phys.* **49** (1987).
[8] K. Binder, *J. Non-Equilib. Thermodyn.* **23** (1998).
[9] G. Brown, A. Chakrabarti, and J. Marko, *Phys. Rev. E* **50** (1994).
[10] S. Tiwari, F. Rana, H. Hanafi, A. Hartstein, E. F. Crabbe, and K. Chan, *Appl. Phys. Lett.* **68**, 1377 (1996).
[11] P. Normand, K. Beltios, E. Kapetanakis, D. Tsoukalas, T. Travlos, J. Stoemenos, J. V. D. Berg, S. Zhang, C. Vieu, H. Launois, et al., *Nucl. Instr. and Meth. in Phys. Res. B* **178**, 74 (2001).
[12] B. De Salvo, G. Ghibaudo, G. Pananakakis, P. Masson, T. Baron, N. Buffet, A. Fernandes, and B. Guillaumot, *IEEE Trans. Electron Devices* **48**, 1789 (2001).
[13] T. Müller, K.-H. Heinig, and W. Möller, *Appl. Phys. Lett.* **81** (2002).
[14] W. Möller and W. Eckstein, *Nucl. Instr. and Meth. in Phys. Res. B* **2**, 814 (1984).
[15] J. F. Ziegler, J. P. Biersack, and U. Littmark, *The Stopping and Range of Ions in Solids* (Pergamon Press, New York, 1985), URL <http://www.srim.org>.
[16] R. Kelly, *Surf. Sci.* **100**, 85 (1980).
[17] W. Möller and M. Posselt, *Wissenschaftlich-Technische Berichte FZR-317, Forschungszentrum Rossendorf* (2001), URL <http://www.fz-rossendorf.de/FWI/FWIT/tridyn.htm>.
[18] M. Strobel, K.-H. Heinig, and W. Möller, *Phys. Rev. B* **64**, 245422 (2001).
[19] N. Metropolis, A. Rosenbluth, M. Rosenbluth, A. Teller, and E. Teller, *J. of Chem. Phys.* **21**, 1087 (1953).